Journal of Solid State Chemistry 182 (2009) 2620–2625

Contents lists available at ScienceDirect

Journal of Solid State Chemistry

journal homepage: www.elsevier.com/locate/jssc

The influence of *A*-site rare-earth for barium substitution on the chemical structure and ferroelectric properties of BZT thin films

C. Ostos [a,b,*], M.L. Martínez-Sarrión [a], L. Mestres [a], E. Delgado [c], P. Prieto [d]

[a] Department of Inorganic Chemistry, University of Barcelona, C/Martí i Franquès, 1-11, 08028 Barcelona, Spain
[b] Center of Nanoscience and Nanotechnology, UNAM, A. Postal 2681, 22800 Ensenada B.C, Mexico
[c] Department of Physics, Universidad del Valle, Building 320-3001, Cali, Colombia
[d] Center of Excellence on Novel Materials, Universidad del Valle, A.A. 25360, Cali, Colombia

ARTICLE INFO

Article history:
Received 1 April 2009
Received in revised form
17 June 2009
Accepted 7 July 2009
Available online 14 July 2009

Keywords:
BZT
Perovskites
Thin films
Magnetron sputtering
Ferroelectrics

ABSTRACT

Rare-earth (*RE*) doped $Ba(Zr,Ti)O_3$ (BZT) thin films were prepared by rf-magnetron sputtering from a $Ba_{0.90}Ln_{0.067}Zr_{0.09}Ti_{0.91}O_3$ (Ln = La, Nd) target. The films were deposited at a substrate temperature of 600 °C in a high oxygen pressure atmosphere. X-ray diffraction (XRD) patterns of *RE*-BZT films revealed a ⟨001⟩ epitaxial crystal growth on Nb-doped $SrTiO_3$, ⟨001⟩ and ⟨011⟩ growth on single-crystal Si, and a ⟨111⟩-preferred orientation on Pt-coated Si substrates. Scanning electron microscopy (SEM) showed uniform growth of the films deposited, along with the presence of crystals of about half-micron size on the film's surface. Transmission electron microscopy (TEM) evidenced high crystalline films with thicknesses of about 100 nm for 30 min of sputtering. Electron-probe microanalysis (EPMA) corroborated the growth rate (3.0–3.5 nm/min) of films deposited on Pt-coated Si substrates. X-ray photoelectron spectroscopy (XPS), in depth profile mode, showed variations in photoelectron Ti 2*p* doublet positions at lower energies with spin-orbital distances characteristic of $BaTiO_3$-based compounds. The XPS analysis revealed that lanthanide ions positioned onto the *A*-site of the BZT-perovskite structure increasing the MO_6-octahedra distortion (M = Ti, Zr) and, thereby, modifying the Ti–O binding length. Polarization-electric field hysteresis loops on Ag/*RE*-doped BZT/Pt capacitor showed good ferroelectric behavior and higher remanent polarization values than corresponding non-doped system.

1. Introduction

Lead-free, $BaTiO_3$-based ceramics show a wide range of properties and have been extensively studied for applications in technologically relevant fields such as micro-electro-mechanical system (MEMS) devices [1]. Among various materials, solid solutions of $Ba(Zr,Ti)O_3$ (BZT) have been used successfully as a basis for such compounds; especially, given their high dielectric constant. On the other hand, the continued drive towards greater miniaturization of electronic components has also led to the development of thin film materials [2,3]. The deposition of BZT-type compounds in thin films has been achieved by a number of physical techniques such as the ablation laser process (PLD) [4–6] and rf-magnetron sputtering (RF) [7–10]. Applications include capacitors for multilayer ceramic capacitors (MLCCs) and ferroelectric random access memories (FRAMs) [11–13].

BZT characteristics have also been improved by inserting a lanthanide ion as dopant [14–16] because of its low leakage current behavior and low electric field. However, extensive studies are still needed on systems where the substitution of a lanthanide ion for barium requires the generation of *A*-site cationic vacancies to maintain electroneutrality in the perovskite structure. Likewise, the control of growth conditions and extensive characterization are crucial in obtaining reproducible and useful materials [17,18]. Hence, we report on the deposition and characterization of high-quality, doped BZT thin films obtained from *A*-site deficient rare-earth (*RE*) doped BZT targets. Our contribution has been focused on the influence of lanthanum and neodymium ions on the chemical structure and ferroelectric properties of *RE*-doped BZT thin films in comparison to non-doped systems. The previous analysis was performed based on X-ray photoelectron spectroscopy results, polarization-electric field hysteresis loops, and leakage current measurements on thin films deposited by RF upon Pt-coated Si substrates.

2. Experimental

Thin film samples were deposited via rf-magnetron sputtering (RF) technique in a high-vacuum system with a base pressure of

* Corresponding author at: Center of Nanoscience and Nanotechnology, UNAM, A. Postal 2681, 22800 Ensenada B.C, Mexico. Fax: +52 1 646 1744603.
E-mail address: ceostoso@cnyn.unam.mx (C. Ostos).

0022-4596/$ - see front matter © 2009 Elsevier Inc. All rights reserved.
doi:10.1016/j.jssc.2009.07.013

5.0×10^{-6} Torr, RF-power of 50–60 W and a target-substrate separation of 220 mm. Ultrahigh purity oxygen was used as the processing gas with a working pressure of $1.5–3.5 \times 10^{-1}$ Torr. The thin films were grown on single-crystal Nb-doped $SrTiO_3$ (100) –Nb:STO–, single-crystal Si (100) –Si– and Pt(111)/TiO_2/SiO_2/Si –Pt– substrates at 600 °C for 15, 30, 45 and 60 min of deposition. Ba(Zr,Ti)O_3 (BZT) thin films were fabricated by using a target with a composition of $BaZr_{0.09}Ti_{0.91}O_3$. Rare-earth (*RE*) doped Ba(Zr,Ti)O_3 thin films were fabricated by using *A*-site deficient rare-earth doped $Ba_{0.90}Ln_{0.067}Zr_{0.09}Ti_{0.91}O_3$ (Ln = La, Nd) targets. The targets were synthesized through a soft chemistry method [19] and sintered at 1450 °C for 3 h. Films were annealed at 600 °C for 30 min in oxygen atmosphere [20].

Films deposited were structurally characterized by X-ray diffraction (XRD) technique in a Phillips MRD diffractometer with parallel optical beam, Cu$K\alpha$ radiation and Bartel-type monochromator. Micro-structural analysis was performed through high-resolution transmission electron microscopy (HRTEM) in a Phillips CM30 microscope coupled to low-energy electron diffraction (LEED) spectrometer. The morphology of the top surface of the films was examined via scanning electron microscopy (SEM) in a LEICA Cambridge S360 microscope, and cross-sections were studied by field emission SEM in an FE-SEM Hitachi S4100 microscope. Film growth was evaluated by electron probe microanalysis (EPMA) in a Cameca SX-50 microscope at 10, 12, 15, and 20 keV. The surface chemistry was analysed by X-ray photoelectron spectroscopy (XPS) in a Perkin Elmer PHI 5500—ESCA System. XPS analysis was performed in depth profile mode and the sputter was achieved by using an Ar^+ ion gun with accelerating voltage of 4 keV and emission current of 15 mA. The ferroelectric polarization and leakage current density of the Ag/*RE*-doped BZT/Pt capacitor system were measured at room temperature by a Precision LC Radiant Technologies System. Hysteresis loops were measured by using a Sawyer-Tower circuit. Silver top electrodes of 6.5×10^{-3} cm^2 area and thickness of 250 nm were deposited by evaporation technique using a shadow mask. The thickness of films grown was determined by the optical interferometry (OI) technique.

3. Results and discussion

X-ray diffraction (XRD) patterns of Nd-doped Ba(Zr,Ti)O_3 thin films deposited on three different substrates after the annealing process are shown in Fig. 1. Rare-earth (*RE*) doped BZT (*RE* = La, Nd) thin films revealed similar crystallographic behavior regardless of whether the lanthanide ion was present or the type of lanthanide.

As shown in Fig. 1a, (100) and (200) reflections, corresponding to the BZT-perovskite phase, are visible for thin films grown on Nb:STO. The diffraction peaks indicate a highly preferred orientation of *RE*-doped BZT films along the *c*-axis. Hence, thin films deposited on a Nb:STO substrate showed good epitaxial crystal growth and high crystalline quality. No second phases were detected. However, film stoichiometry with high content of zirconium was found by using Vegard's law ($Pm3m$; $a = 4.176(1)$ Å). This fact could be explained as a consequence of the ideal tolerance factor ($t = 1$) calculated for $SrTiO_3$ and $BaZrO_3$ structures when the crystal symmetry is cubic. Nevertheless, caution should be taken because Bragg peak positions from thin-film specimens might be shifted due to intrinsic stresses and, thereby, intrinsic strains. Anyhow, these films can be useful for applications in tunable-ceramic capacitors given their possible relaxor-like ferroelectric behavior at low temperatures [21,22].

For thin films grown on Pt, the XRD pattern (Fig. 1b) showed a (111)-plane orientation because a high-purity commercial Pt-coated Si substrate with a [111]-preferred orientation was used. No additional reflection or second phases were detected. The reflection observed corresponds to the BZT-perovskite phase with a Bragg peak position similar to that observed for the powder used as target. It might indicate that the films exhibited a closer

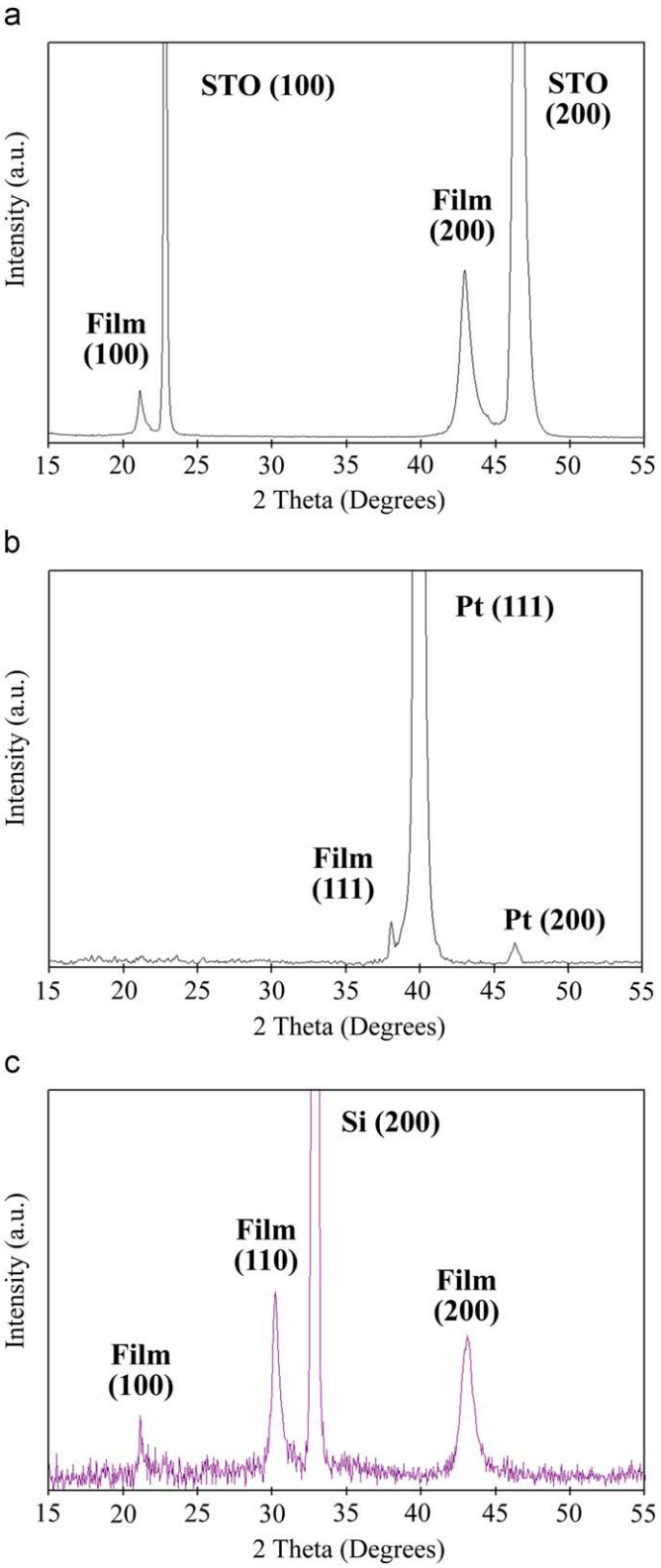

Fig. 1. XRD patterns of Nd-doped BZT thin films grown on (a) Nb:STO, (b) Pt and (c) Si substrates for 45 min of deposition.

stoichiometry with respect to the target. Since the peak position can be affected by mechanical reasons and not only in terms of chemical composition, the stoichiometry of the films deposited was found by high-resolution X-ray photoelectron spectroscopy (XPS). The XPS analysis performed in depth profile mode, showed homogeneous composition distribution throughout the whole film until reaching the substrate, and an excess of zirconium about 10 at% in the nominal composition of the films deposited.

For thin films grown on Si, the XRD pattern (Fig. 1c) showed (100), (110), and (200)-perovskite reflections in spite of the fact that a Si substrate with a (100)-plane orientation was used. No second phases were detected. As noted on the Nb:STO system, films grown on Si also experienced difficulties in obtaining a titanium-rich perovskite single phase because the diffraction peaks shifted toward a lower angle. This fact could be due to the difference between silicon lattice parameters ($Fm3m$, $a = 5.3920$ Å) and those of the perovskite ($Pm3m$; $a = 4.02$ Å), and the mismatch of crystal structures as a result of the re-structuring of the substrate atoms to (2×1)-type dimmers. Another feasible way to explain this crystallographic behavior is the SiO_2 interface formation of a few nanometers thick by which the coupling between the film deposited and the substrate differs. Thus, Fig. 2 shows the microstructure analysis of thin films deposited on Si via cross-section, high-resolution transmission electron microscopy (HRTEM) technique.

Fig. 2a shows a HRTEM micrograph for a crystalline thin film with (100) and (110) interplanar distance values of 4.14 and 2.95 Å, respectively. Spacings were determined from a fast Fourier transform on the sized regions of interest by using the Digital Micrograph™ 3.7.4 software. Additionally, two different interfaces for films deposited on Si were observed. The interfaces correspond to SiO_x and an amorphous film layer of about 10 nm each one. The high-polycrystalline film with $BaTiO_3$-based perovskite structure was evidenced by the low-energy electron diffraction (LEED) pattern in Fig. 2b.

Fig. 3 shows both scanning electron microscopy (SEM) on the film's surface and cross-section field-emission (FE) SEM micrographs. SEM analysis of the film's surface (Fig. 3a) revealed that cracks and holes were not present in an analysis area of 150 μm^2, and the presence of crystal sizes in the range of 0.1 μm up to 0.5 μm as a result of annealing process. The cross section FE-SEM micrograph (Fig. 3b) evidenced uniform growth of the film across the surface of the substrate and a thickness about 200 nm at 60 min of deposition. Similar morphological behavior was observed for films grown on the other two substrates tested.

From previously discussed results and because platinum is a good candidate for use as a bottom electrode [23], the *RE*-doped BZT/Pt system was chosen for further characterization. The corresponding results are shown hereinafter.

The growth of *RE*-doped BZT films was evaluated by electron-probe microanalysis (EPMA) by using a high-energy electron beam. EPMA data are shown in Table 1. Depth mass ($\mu g\,cm^{-2}$) depends only on the energy of the electron bombardment required to detect platinum on the top surface of the Pt-coated Si substrate. Film thickness was calculated with a theoretical density of 6.0 $g\,cm^{-3}$. The growth rate of the samples deposited was determined about 3–3.5 nm per minute of deposition under experimental RF conditions.

Fig. 4 shows the XPS composition distribution of the surface layers of samples deposited on Pt after 1 min of 4 keV Ar^+ sputter cleaning. Short etching times avoid possible secondary effects on the composition, chemical environment and structural changes of the thin films. The peak of C 1*s* at 284.80 eV was assigned to carbon contamination and was used as the criterion to rectify the energy of spectra. The binding energy of the Ar 2*p*-signal at 241.46 eV was caused by the argon sputtering [24]. XPS photoelectron lines of the films deposited coincided with the chemical states for a $BaTiO_3$-based compound (Fig. 4a). The Ba 3*d* doublet consists of two peaks at 779.3 and 794.7 eV, identified as signals from Ba–O bonds with a real spin–orbit distance (Δ) between the two peaks of 14.6 eV. The Zr 3*s* signal was fitted at 431.1 eV, and the Zr 3*p* doublet consists of two peaks of Zr $3p_{1/2}$ at 345.7 eV and Zr $3p_{3/2}$ at 331.9 eV ($\Delta = 13.8$ eV). The O 1*s* signal was fitted at 530.81 eV. For the La-doped BZT film (Fig. 4b), the La 3*d* doublet was identified and fitted at 851.4 and 833.7 eV ($\Delta = 17.7$ eV) for the La $3d_{3/2}$ and La $3d_{5/2}$ signals, respectively. Similarly, the XPS survey spectrum of the Nd-doped BZT film (Fig. 4c) showed the Nd 3*d* doublet fitted at 1004.0 and 981.5 eV ($\Delta = 22.5$ eV) for the Nd $3d_{3/2}$ and Nd $3d_{5/2}$ signals, respectively. The chemical shifts and spin orbit separation energies of the Ti 2*p* doublet were calculated when the exact peak position was definite. XPS technique is extremely sensitive to chemical changes occurring on related $BaTiO_3$ surfaces.

Fig. 5 illustrates the fitted Ti 2*p* narrow-scan spectra, i.e. fitting bands and convolution curves for spectra simulation, by asymmetrical Gaussian–Lorentzial sum function. The *Multipak* software was used to fit the narrow-scan spectra after Shirley-type background subtraction for each film deposited. The Ti 2*p* peak is composed of the Ti $2p_{1/2}$ peak at higher binding energy and the Ti $2p_{3/2}$ peak at lower binding energy; both of them belong to Ti–O bonds. XPS photoelectron positions of the Ti 2*p* peaks are summarized in Table 1. In Fig. 5a, the Ti 2*p* doublet could be fitted into two pairs of peaks centered at 464.36 and 462.20 eV for Ti $2p_{1/2}$ peaks, and at 458.99 and 456.76 eV for Ti

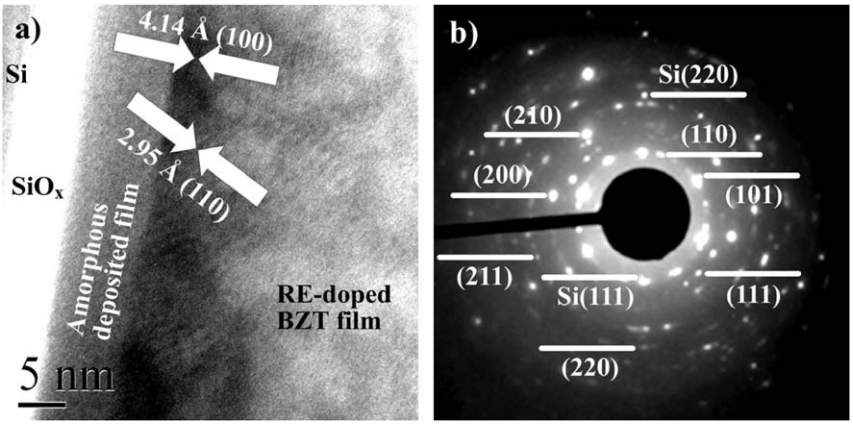

Fig. 2. (a) HRTEM micrograph and (b) low-energy electron diffraction of a Nd-doped BZT film deposited on Si substrate.

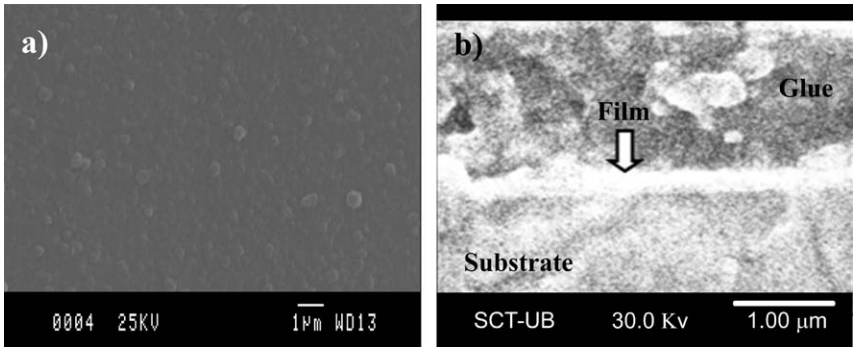

Fig. 3. (a) SEM micrograph of the film's surface and (b) cross-section FE-SEM micrograph of a Nd-doped BZT thin film deposited on Si substrate.

Table 1
XPS photoelectron positions of Ti 2*p* doublets for BZT, La-doped BZT and Nd-doped BZT thin films.

	1st Doublet		2nd Doublet		3rd Doublet		Depth			
	$2p_{1/2}$ (eV)	$2p_{3/2}$ (eV)	$2p_{1/2}$ (eV)	$2p_{3/2}$ (eV)	$2p_{1/2}$ (eV)	$2p_{3/2}$ (eV)	P_r (μC cm^{-2})	E_c (kV cm^{-1})	Mass[a] (μg cm^{-2})	Thickness[a] (nm)
BZT	464.36 [$\Delta = 5.37$ eV]	458.99	462.20 [$\Delta = 5.44$ eV]	456.76	–	–	4.19	50.5	25.000	150.000
La-BZT	464.21 [$\Delta = 5.44$ eV]	458.77	460.26 [$\Delta = 5.39$ eV]	454.87	–	–	4.81	43.6	21.990	131.940
Nd-BZT	464.21 [$\Delta = 5.39$ eV]	458.82	462.27 [$\Delta = 5.37$ eV]	456.90	459.14 [$\Delta = 5.37$ eV]	453.77	5.71	67.7	26.320	157.920

Remanent polarization (P_r) and coercive field (E_c) for the Ag/*RE*-doped BZT/Pt capacitors at room temperature.

[a] EPMA microanalysis of *RE*-doped BZT samples grown on Pt for 45 min of deposition.

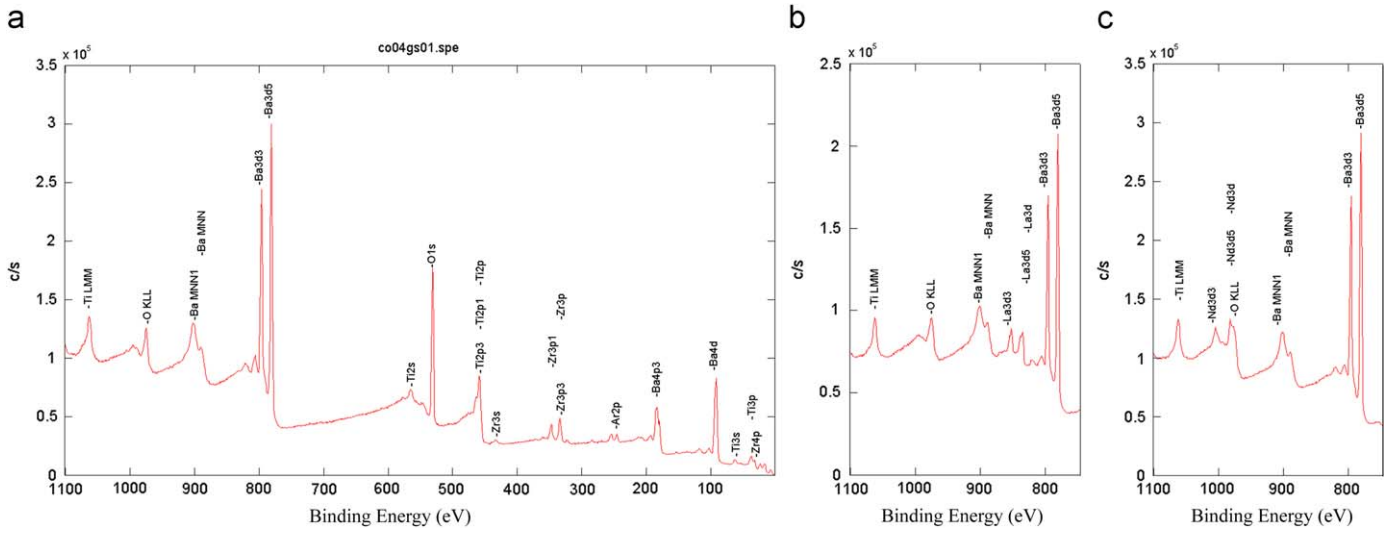

Fig. 4. XPS survey spectra of (a) BZT, (b) La-doped BZT and (c) Nd-doped BZT thin films grown on Pt substrate. The samples were etched for 1 min with a 4keV Ar+ sputter gun.

$2p_{3/2}$ peaks, respectively. A similar fit for La-doped samples is illustrated in Fig. 5b; however, the peaks shift towards lower binding energy regions and the full width at half maximum (FWHM) of the peak becomes wide. This fact may be explained by the variations of the titanium chemical environment, mainly related to shifts of the Ti–O binding energy in the MO_6 (M = Zr, Ti) perovskite octahedra. In Fig. 5c, the Ti 2*p* doublet could be fitted into three pairs of Ti $2p_{1/2}$ and Ti $2p_{3/2}$ peaks with usual spin–orbital distances characteristic of a $BaTiO_3$-based structure ($\Delta \approx 5.4$ eV). The first two pairs of peaks are at closer positions to those determined for a non-doped BZT system. The third Ti 2*p* doublet is centered at 459.14 and 453.77 eV for Ti $2p_{1/2}$ and Ti $2p_{3/2}$ peaks, respectively. These results are related to the combined effect of zirconium for titanium substitution, the *A*-site cationic vacancies that could have been created when barium was substituted by the lanthanide ion and the presence of the rare-earth element by itself. Thus, the MO_6 octahedra are distorted, the unit cells of the perovskite structure are stressed and, therefore, the Ti–O binding length differs between them. Moreover, the lanthanide ion because of its lower ionic radius and higher charge (3+) than that of barium increases the ionic character of A–O bonds (ABO_3) and, thereby, decreases the covalent character of

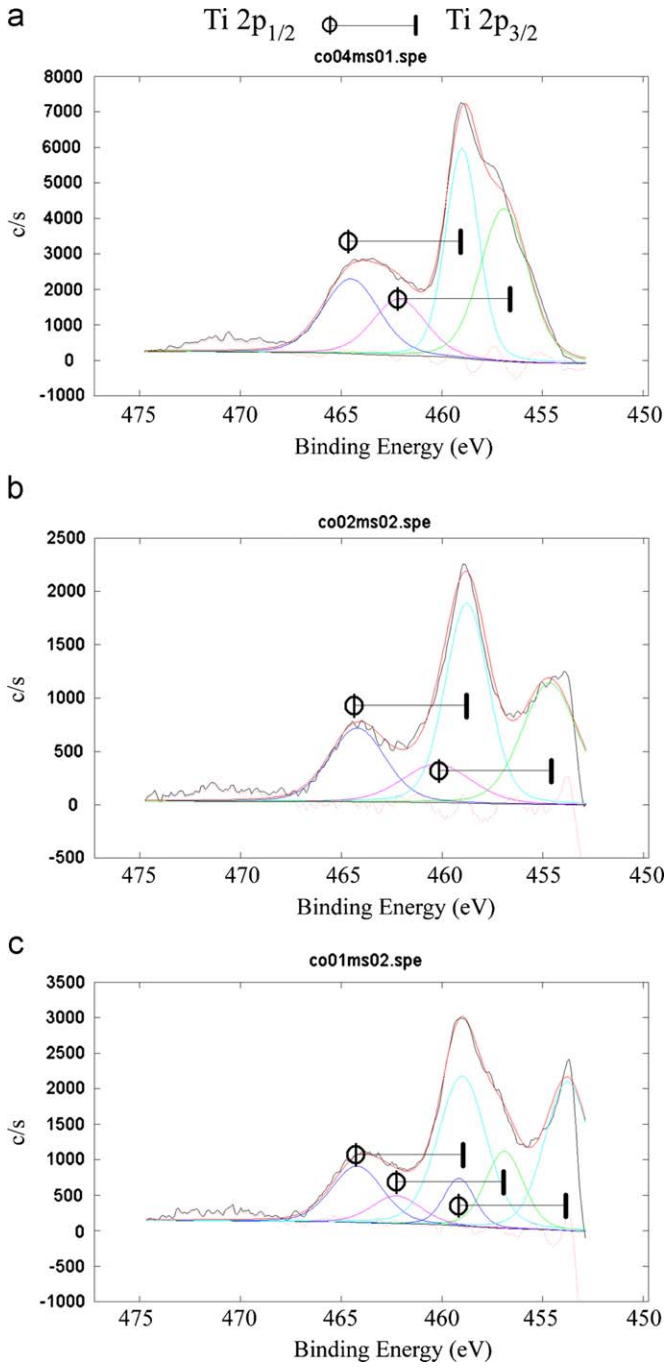

Fig. 5. XPS narrow-scan spectra of Ti 2*p* doublets of the (a) BZT, (b) La-doped BZT and (c) Nd-doped BZT films deposited on Pt substrate.

Ti–O bonds because of its higher polarizing force. This effect is remarkably stronger in neodymium than in lanthanum doped samples and, due to this, the Ti 2*p* doublet of Nd-doped samples present three differentiated pairs of peaks instead of two. It seems probable that the neodymium dopant causes the most positive effect in achieving large spontaneous polarization when it is positioned into the BZT perovskite structure.

Fig. 6 shows the polarization vs. electric field (*P*–*E*) hysteresis loops for the Ag/RE-doped BZT/Pt system obtained by applying triangular voltage at a frequency of 10 kHz. Values of remanent polarization (P_r) and coercive field (E_c) are shown in Table 1. The shape of the P–E hysteresis loops indicates the ferroelectricity of the thin films deposited and a usual non-ohmic contact, characteristic of an asymmetric device. For non-doped and

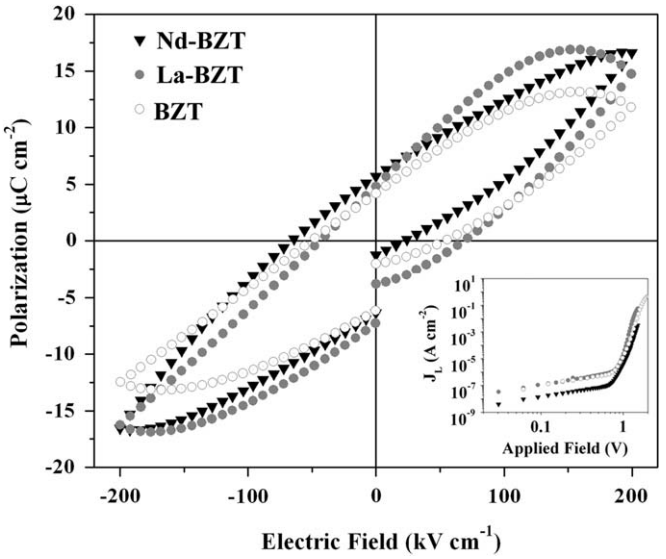

Fig. 6. Polarization vs. electric field (*P*-*E*) loops at room temperature for the Ag/ RE-doped BZT/ Pt capacitor system. The inset represents the dc leakage current vs voltage behavior (*J*-*V*).

La-doped BZT films, the P–E hysteresis loops seem linear due to the existence of permanent electric dipoles created bellow the Curie temperature. In this state, the dielectric is not a good isolator and it is an unstable linear capacitor in order to retain memory. However, neodymium-doped samples showed good ferroelectric behavior because electric dipoles are not proportional to the applied electric field. This is characteristic of materials useful as capacitors for memory applications. Nevertheless, when a voltage is applied to a ferroelectric capacitor, the current flowing through the external circuit is comprised of two components, polarization contribution and leakage contribution. Losses result in a cigar-shaped loop as occurs for non-doped and La-doped samples.

The inset of Fig. 6 shows the variation in dc leakage current versus applied voltage at room temperature for the thin films deposited on Pt. Measurements were run with a delay time of 100 ms. The I–V loops showed a low-current density and the leakage current begins with a linear dependence with voltage, as can be seen from its slope in the log–log plot, but at a voltage above 2 V the capacitor begins to get saturated. For this reason, the *P*–*E* ferroelectric measurements were recorded up to a voltage of 2 V and because of this, the ferroelectric nature of RE-doped BZT films could be confirmed. Different conduction mechanisms such as Schottky-type conduction and space charge limited conduction (SCLC) may explain the nature of charge transport phenomena in the BZT-type thin films [25–28]. However, ferroelectric thin films are extremely complex electric systems and the effects caused by the ferroelectric polarization are overlapped or interacted with the chemistry defects of the material, the interfacial electronic states, and the film microstructure [29].

4. Conclusions

In summary, *RE*-doped BZT (*RE* = La, Nd) thin films were deposited by rf-magnetron sputtering from a well-sintered $Ba_{0.90}Ln_{0.067}Zr_{0.09}Ti_{0.91}O_3$ target. The crystallographic behavior of each system depended mainly on the substrate upon which the thin films were grown, regardless of the presence or the type of lanthanide. The films deposited revealed uniform growth, the presence of crystals of about half-micron size on the film's surface, and highly crystalline films with thicknesses near 100 nm for

30 min of sputtering. Rare-earth ions positioned onto the *A*-site of the BZT-perovskite structure increasing the MO_6-octahedra distortion (M = Ti, Zr) and, therefore, modifying the Ti–O binding length. Results demonstrated that *RE*-doped BZT thin films are ferroelectric materials and exhibit up to 36% larger remanent polarization than non-doped ones. In this study, the neodymium dopant is considered the best alternative for improving the BZT ferroelectric properties according to the microstructural analysis done via XPS.

Acknowledgments

This research was supported by the CICYT of Spain through the MAT 2007-63445 project, DGAPA IN102908, IN114207 and IN109608 projects, CONACYT 82503 project and the Center of Excellence on Novel Materials through COLCIENCIAS contract 043-2005. C. Ostos thanks the UNAM for the research grant. The authors gratefully acknowledge the technical support provided by the *Serveis Cientifico-Técnics* of the University of Barcelona and for the ferroelectric measurements conducted by the Thin Film Laboratory at West Virginia University in the United States.

References

[1] Y. Sakai, T. Futakuchi, T. Iijima, M. Adachi, Jpn. J. Appl. Phys. 44 (5A) (2005) 3099–3102.
[2] W.S. Choi, B.S. Jang, D.-G. Lim, J. Yi, B. Hong, J. Cryst. Growth 237–239 (2002) 438–442.
[3] C.-S. Hsi, C.-Y. Chen, M.-C. Wang, J. Appl. Phys. 94 (1) (2003) 598–604.
[4] S. Halder, S.B. Krupanidhi, Solid State Commun. 122 (2002) 429–432.
[5] T. Kawahara, T. Ohno, A. Doi, H. Tabata, T. Kawai, T. Hino, Jpn. J., Appl. Phys. 45 (5B) (2006) 4484–4488.
[6] W.J. Jie, J. Zhum, W.F. Qin, X.H. Wei, J. Xiong, Y. Zhang, A. Bhalla, R. Li, J. Phys. D Appl. Phys. 40 (2007) 2854–2857.
[7] W.J. Leng, C.R. Yang, H.W. Chen, H. Ji, C.L. Fu, J.X. Liao, J. Appl. Phys. 99 (2006) 114904-08.
[8] Y.K.V. Reddy, D. Mergel, S. Reuter, V. Buck, M. Sulkowski, J. Phys. D: Appl. Phys. 39 (2006) 1161–1168.
[9] W.S. Choi, B.S. Jang, Y. Roh, R. Yi, B. Hong, J. Non-Cryst. Solids 303 (2002) 190–193.
[10] W.S. Choi, J.-H Boo, J. Yi, B. Hong, Mater. Sci. Semicond. Process. 5 (2003) 211–216.
[11] J.F. Scott, C.A. Paz de Araujo, Science 246 (1989) 1400–1405.
[12] D. Hennings, R. Waser, U. Weber, G. Greuel, U. Boettger, S. Weber, J. Am. Ceram. Soc. 84 (4) (2001) 759–766.
[13] B.W. Ricketts, G. Triani, A.D. Hilton, J. Mater. Sci. Mater. Electron. 11 (2000) 513.
[14] C. Ostos, M.L. Martínez-Sarrión, L. Mestres, A. Cortés, E. Delgado, P. Prieto, Braz. J. Phys. 36 (3B) (2006) 1062–1065.
[15] E. Delgado, C. Ostos, M.L. Martínez-Sarrión, L. Mestres, P. Prieto, Phys. Status Solidi C 4 (11) (2007) 4099–4106.
[16] W.S. Choi, J. Yi, B. Hong, Mater. Sci. Eng. B 109 (2004) 146–151.
[17] H.-H. Huang, M.-C. Wang, C.-Y. Chen, N.-C. Wu, H.-J. Lin, J. Eur. Ceram. Soc. 26 (2006) 3211–3219.
[18] K.V. Saravanan, K. Sudheendran, M.G. Krishna, K.C.J. Raju, A.K. Bhatnagar, Vacuum 81 (2006) 307–316.
[19] C. Ostos, M.L. Martínez-Sarrión, L. Mestres, J.E. García, A. Albareda, R. Perez, Solid State Sci. 11 (2009) 1016–1022.
[20] J.X. Liao, C.R. Yang, Z. Tian, H.G. Yang, L. Jin, J. Phys. D Appl. Phys. 39 (2006) 2473–2479.
[21] T. Maiti, R. Guo, A.S. Bhalla, Appl. Phys. Lett. 90 (2007) 182901-1-3.
[22] T. Maiti, R. Guo, A.S. Bhalla, Appl. Phys. Lett. 89 (2006) 122909-1-3.
[23] V. Reymond, O. Bidault, D. Michau, M. Maglione, P. Payan, J. Phys. D Appl. Phys. 39 (2006) 1204–1210.
[24] S. Hofmann, Philos. Trans. R. Soc. London Ser. A 362 (2004) 55–75.
[25] C. Sudhama, A.C. Campbell, P.D. Manier, R.E. Jones, R. Moazzami, C.J. Mogab, J. Lee, J. Appl. Phys. 75 (1994) 1014–1023.
[26] J.F. Scott, B.M. Melnick, J.D. Cuchiaro, R. Juleeg, C.A. Paz de Araujo, A.D. McMillan, M.C. Scott, Integr. Ferroelectr. 4 (1994) 85–92.
[27] T. Mihara, H. Watanabe, Jpn. J. Appl. Phys. 34 (1995) 5664–5673.
[28] I. Stolichnov, A. Tagantsev, J. Appl. Phys. 84 (1998) 3216–3225.
[29] C.A. Paz de Araujo, J.F. Scott, G.W. Taylor, Ferroelectric Thin Films: Synthesis and Properties, Gordon and Breach Publishers, Amsterdam, 1996.